The Brain of LB1, Homo floresiensis

Dean Falk, *et al.*

Science **308**, 242 (2005);
DOI: 10.1126/science.1109727

before the cap carbonate precipitated. This may explain the lack of a sharp Ir spike at the base of the Sturtian cap carbonate. Alternatively, during the Sturtian glacial epoch, Earth's surface may not have been fully covered with ice on which extraterrestrial material could accumulate for a long time; however, the presence of banded iron formations in and below Sturtian glacials suggests that the ocean was ice-covered at that time (*3*).

References and Notes

1. J. L. Kirschvink, in *The Proterozoic Biosphere*, J. W. Schopf, C. Klein, Eds. (Cambridge Univ. Press, Cambridge, 1992), pp. 51–52.
2. P. F. Hoffman, A. J. Kaufman, G. P. Halverson, D. P. Schrag, *Science* **281**, 1342 (1998).
3. P. E. Hoffman, D. P. Schrag, *Terra Nova* **14**, 129 (2002).
4. W. T. Hyde, T. J. Crowley, S. K. Baum, W. R. Peltier, *Nature* **405**, 425 (2000).
5. T. J. Crowley, W. T. Hyde, W. R. Peltier, *Geophys. Res. Lett.* **28**, 283 (2001).
6. K. Caldeira, J. F. Kasting, *Nature* **359**, 226 (1992).
7. K. Caldeira, *Geology* **19**, 204 (1991).
8. L. E. Sohl, N. Christie-Blick, D. V. Kent, *Geol. Soc. Am. Bull.* **111**, 1120 (1999).
9. Materials and methods are available as supporting material on *Science* Online.
10. C. Koeberl, H. Huber, *J. Radioanal. Nucl. Chem.* **244**, 655 (2000).
11. J. T. Wasson, in *Meteorites: Their Record of Solar System History* (Freeman, New York, 1985), p. 267.
12. Z. Ceplecha, *Astron. Astrophys.* **263**, 361 (1992).
13. K. A. Parley, D. B. Patterson, *Nature* **378**, 600 (1995).
14. F. T. Kyte, J. T. Wasson, *Science* **232**, 1225 (1986).
15. E. Anders, N. Grevesse, *Geochim. Cosmochim. Acta* **53**, 197 (1989).
16. H. Heinrich, *Quat. Res.* **29**, 142 (1988).
17. J. D. Roberts, *J. Geol.* **84**, 47 (1974).
18. I. J. Fairchild, in *Sedimentology Review*, V. P. Wright, Ed. (Blackwell, Oxford, 1993), pp. 1–16.
19. M. J. Kennedy, *J. Sediment. Res.* **66**, 1050 (1996).
20. D. C. Noble, W. L. Rigot, H. R. Bowman, *GSA Spec. Pap.* **180**, 77 (1979).
21. Basaltic Volcanism Study Project, in *Basaltic Volcanism on the Terrestrial Planets* (Pergamon, New York, 1981), p. 1286.
22. B. Peucker-Ehrenbrink, *Geochim. Cosmochim. Acta* **60**, 3192 (1996).
23. F. Marcantonio *et al.*, *Nature* **383**, 705 (1996).
24. F. Marcantonio *et al.*, *Geochim. Cosmochim. Acta*. **62**, 1535 (1998).
25. F. Marcantonio *et al.*, *Earth Planet. Sci. Lett.* **170**, 157 (1999).
26. B. Schmitz, B. Peucker-Ehrenbrink, M. Lindström, M. Tassinari, *Science* **278**, 88 (1997).
27. A. H. Knoll, M. R. Walter, *Nature* **356**, 673 (1992).
28. J. P. Grotzinger, S. A. Bowring, B. Z. Saylor, A. J. Kaufman, *Science* **270**, 598 (1995).
29. H. Porada, *Precambrian Res.* **44**, 103 (1989).
30. R. M. Key *et al.*, *J. Afr. Earth Sci.* **33**, 503 (2001).

31. We thank H. Rice and F. Popp from the University of Vienna for discussions and comments. This work was supported by the Austrian Science Foundation. This is University of the Witwatersrand Impact Cratering Research Group publication no. 93.

Supporting Online Material

www.sciencemag.org/cgi/content/full/308/5719/239/DC1
Materials and Methods
Fig. S1
Tables S1 to S3
References and Notes

30 August 2004; accepted 18 January 2005
10.1126/science.1104657

The Brain of LB1, *Homo floresiensis*

Dean Falk,[1]* Charles Hildebolt,[2] Kirk Smith,[2] M. J. Morwood,[3] Thomas Sutikna,[4] Peter Brown,[3] Jatmiko,[4] E. Wayhu Saptomo,[4] Barry Brunsden,[2] Fred Prior[2]

The brain of *Homo floresiensis* was assessed by comparing a virtual endocast from the type specimen (LB1) with endocasts from great apes, *Homo erectus*, *Homo sapiens*, a human pygmy, a human microcephalic, specimen number Sts 5 (*Australopithecus africanus*), and specimen number WT 17000 (*Paranthropus aethiopicus*). Morphometric, allometric, and shape data indicate that LB1 is not a microcephalic or pygmy. LB1's brain/body size ratio scales like that of an australopithecine, but its endocast shape resembles that of *Homo erectus*. LB1 has derived frontal and temporal lobes and a lunate sulcus in a derived position, which are consistent with capabilities for higher cognitive processing.

The type specimen of *Homo floresiensis* (LB1, female) (*1*) has a brain size of ~400 cm^3, which is similar to that of *Australopithecus afarensis* specimen AL 288-1 (Lucy) (*2*), who lived approximately 3.0 million years ago. Yet LB1's species was associated with big-game stone technology, remains of *Stegodon*, and charred animal bones that hint at the use of fire and cooking. Its ancestors also had to cross the sea to reach the Indonesian island of Flores (*3*). Could a tiny hominin with an ape-sized brain really have engaged in such advanced behaviors? Some workers reject the notion that LB1 represents a new species that was closely tied to *H. erectus* (*1*) and suggest instead that it was a pathological human microcephalic (*4*). To help address this debate, we compared three-dimensional computed tomographic (3DCT) reconstructions of the internal braincase (virtual endocasts) that reproduce details of external brain morphology, including sulci, vessels, sinuses, cranial capacity, and shape (*5*–*8*), from LB1, an adult female chimpanzee, an adult female *H. erectus* (specimen ZKD XI), a contemporary woman, and a European microcephalic. To broaden taxonomic comparisons and supplement limited sample size, our analysis also included endocasts of the skulls of specimen Sts 5 (*A. africanus*), specimen KNM-WT 17000 (*Paranthropus aethiopicus*), 10 humans, 10 gorillas, 18 chimpanzees (*9*), an adult female pygmy, and five *H. erectus*.

Our virtual cranial capacity estimate for LB1 is 417 cm^3 (*10*). Virtual endocasts of the microcephalic, modern woman, *H. erectus*, and chimpanzee were scaled to 417 cm^3 to facilitate shape comparisons (Fig. 1 and fig. S2). LB1's shape most resembles that of ZKD XI, which is typical of classic *H. erectus* from China and Java (Trinil) (fig. S3). Both endocasts are noticeably wider caudally than rostrally (Fig. 1A), wider ventrally than dorsally (fig. S2), and relatively long and low in lateral profile (Fig. 1B). However, LB1 lacks the de-

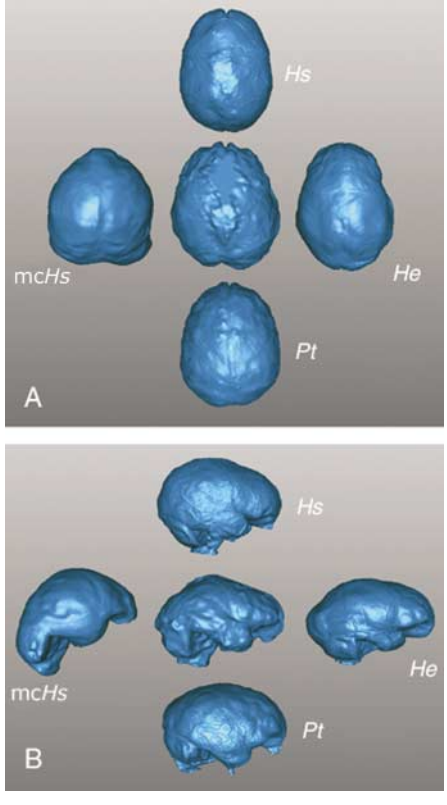

Fig. 1. Comparisons of virtual endocasts of LB1 (center). (**A**) Dorsal views. (**B**) Right lateral views. *Hs*, *H. sapiens*; *Pt*, *Pan troglodytes*; mc*Hs*, a human microcephalic; *He*, *H. erectus*.

[1]Department of Anthropology, Florida State University, Tallahassee, FL 32306, USA. [2]Mallinckrodt Institute of Radiology, Washington University School of Medicine, St. Louis, MO 63110, USA. [3]Archaeology and Palaeoanthropology, University of New England, Armidale, New South Wales 2351, Australia. [4]Indonesian Centre for Archaeology, Jl. Raya Condet Pejaten No. 4, Jakarta 12001, Indonesia.

*To whom correspondence should be addressed. E-mail: dfalk@fsu.edu

rived occipital expansion over the cerebellum of *H. erectus* (Fig. 1B), and its endocast is relatively wider (more brachycephalic) (Fig. 1A and fig. S3). LB1's endocast least resembles the microcephalic's (Fig. 1 and fig. S2), which has a pointed frontal lobe, compressed occipital lobe, and flattened posterior end, with the caudalmost poles on the cerebellum. Although our sample includes only one microcephalic endocast, its shape conforms to features of its corresponding skull that typify primary microcephaly (microcephalia vera): small cranial vault relative to face, sloping forehead, and pointed vertex (*11*, *12*). The only criterion for secondary microcephaly is an occipitofrontal circumference below –2 SD for age and sex (*11*), but these data are unavailable for LB1's population. Unless a *H. erectus*–like endocast shape is characteristic of an unrecognized form of secondary microcephaly, we reject the hypothesis that LB1 was a pathological microcephalic (*4*).

Length, breadth, height, and frontal breadth measurements were collected from endocasts (Table 1 and table S1) and used to generate six ratios (Table 1). In a principal-components analysis, LB1 groups with *H. erectus* and is separate from *H. sapiens*, Sts 5 (fig. S4), and the pygmy, based on the first principal component (weighted heavily on relative height and the disparity between maximum breadth and frontal breadth), and is separate from *H. erectus* and the microcephalic in the second principal component (weighted heavily on breadth relative to length) (Fig. 2A). LB1 bears little resemblance to the pygmy (fig. S5). Typically, pygmy skulls are over 1000 cm^3 (ours measures 1249 cm^3) and resemble those of neighboring humans in shape (*13*). Unlike LB1, whose brain/body size ratio scales like that of an australopithecine, however, the ratio for pygmies is slightly larger than that found in

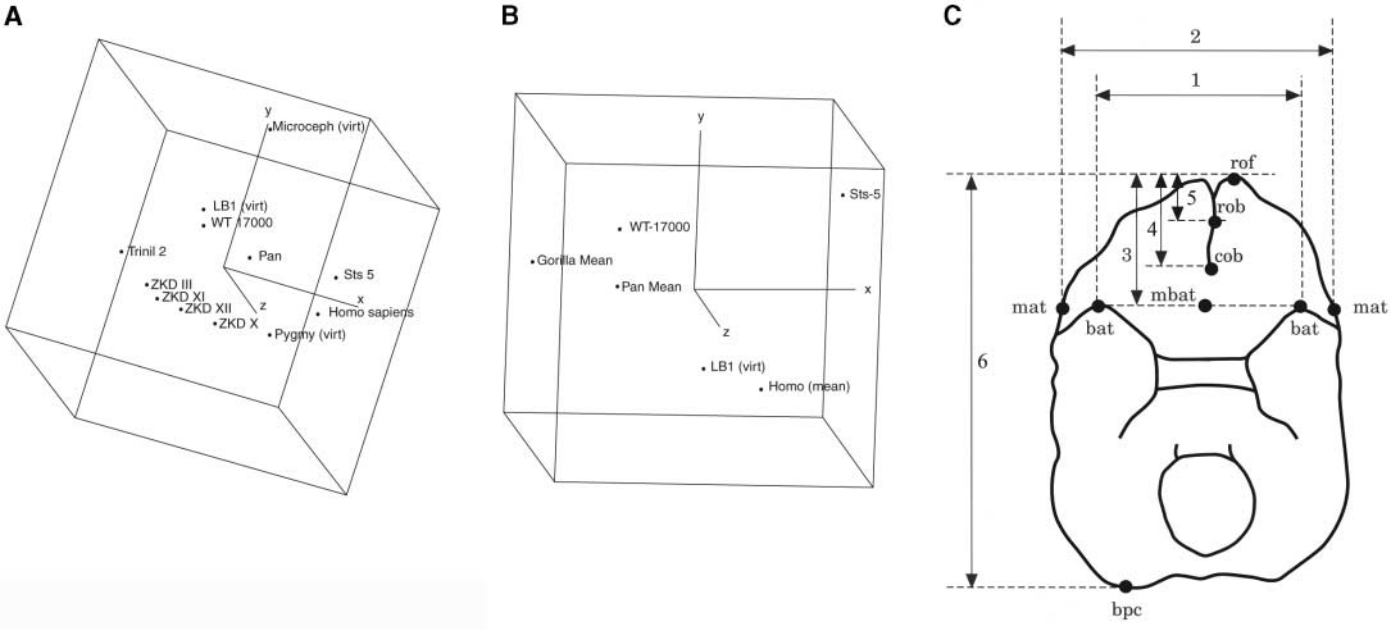

Fig. 2. Plots of principal components and key for basal view measurements. (**A**) Plots of the first three principal components resulting from the analysis of the endocast indices listed in Table 1 [excluding B-FB/H, which was highly correlated with B-FB/L (r = 0.98)]. First, second, and third principal components are aligned along the x, y, and z axes. (**B**) Plots of the first three principal components resulting from the analysis of basal-view endocast indices listed in table S2. (**C**) Key for basal view data analyzed in (B) (*9*). Measurements obtained from basal views were projected onto the horizontal (basal) plane from endocasts. Landmarks: bat, most anterior point on temporal lobe from basal view; mat, most lateral point on endocast at the level of bat in basal plane; mbat, middle of the line connecting the two bats; rof, the most rostral point on the orbital surfaces of the frontal lobes; cob, caudal boundary of olfactory bulbs (cribriform plate) in the midline; rob, rostral boundary of olfactory bulbs in the midline; bcp, most posterior point on the cerebellum in basal view.

Table 1. Endocast measurements (in mm) of length, breadth, height, frontal breadth, and resulting indices.

	Length	Breadth	Height	Frontal breadth	Breadth/ length	Height/ length	Frontal breadth/ length	(Breadth – frontal breadth)/ length	(Breadth – frontal breadth)/ height	Height/ breadth
Pan troglodytes (n = 7)	108.8	88	75.3	72.8	0.81	0.69	0.67	0.14	0.20	0.86
H. sapiens (n = 7)	168.0	128.0	122.0	114.0	0.76	0.73	0.68	0.08	0.11	0.95
KNM-WT 17000*	113.4	92.9	72.5	78.1	0.82	0.64	0.69	0.13	0.20	0.78
Sts 5†	119.1	93.5	86.3	85.6	0.79	0.72	0.72	0.07	0.09	0.92
ZKD III (skull E1)‡	158.6	124.5	99.7	91.4	0.78	0.63	0.58	0.21	0.33	0.80
ZKD X (skull LI)‡	174.6	130.4	114.9	106.7	0.75	0.66	0.61	0.14	0.21	0.88
ZKD XI (skull LII)‡	165.9	127.2	103.7	97.1	0.77	0.63	0.59	0.18	0.29	0.82
ZKD XII (skull LIII)‡	167.4	128	108.5	97.8	0.76	0.65	0.58	0.18	0.28	0.85
Trinil 2§	156.7	126.9	95	92.5	0.81	0.61	0.59	0.22	0.36	0.75
Microcephalic‖	89.1	84.4	66.3	63.7	0.95	0.74	0.71	0.23	0.31	0.79
Pygmy‖	165.7	123.9	116.9	102.6	0.75	0.71	0.62	0.13	0.18	0.94
LB1‖	119.6	102.8	81.4	77.7	0.86	0.68	0.65	0.21	0.31	0.79

**Paranthropus aethiopicus.* †*A. africanus.* ‡*H. erectus* (formerly *Sinanthropus*, China). §*H. erectus* (formerly *Pithecanthropus*, Java). ‖Computer model, virtual endocast.

their nonpygmy neighbors, giving their heads a relatively large appearance (*14*). This is expected because pygmies scale allometrically along ontogenetic curves (*15*), leading to relatively enlarged heads and brains, as is the case for human youngsters relative to adults (*16*) (fig. S1). The laws governing allometric scaling of brain/body ratios are powerful and hold within other species of primates (*17*, *18*). For this reason, and because the morphologies of our endocast samples differ greatly, we do not believe that LB1 represents a human pygmy (*19*).

A second principal-components analysis was performed on measurements from the base of LB1's endocast and compared to similar measurements from 10 gorillas, 18 chimpanzees, 10 *H. sapiens*, KNM-WT 17000 (*Paranthropus aethiopicus*), and Sts 5 (*9*) (Fig. 2, B and C, and tables S2 and S3). The *H. erectus* endocasts were excluded because their bases were missing. The first and second principal-components analyses group LB1 exclusively with *H. sapiens* (Fig. 2B). The first principal component is most heavily weighted on 4/6 and 5/6 (Fig. 2C), which represent the relative projection of the prefrontal cortex rostral to both the anterior and posterior margins of the olfactory bulb. The second principal component is most heavily weighted on 3/6 and (6-3)/6, which represent the relative length of the frontal lobes rostral to the temporal poles and the relative length of the brain caudal to the temporal poles. As in humans, the most anterior sectors of LB1's orbital surfaces are lengthened.

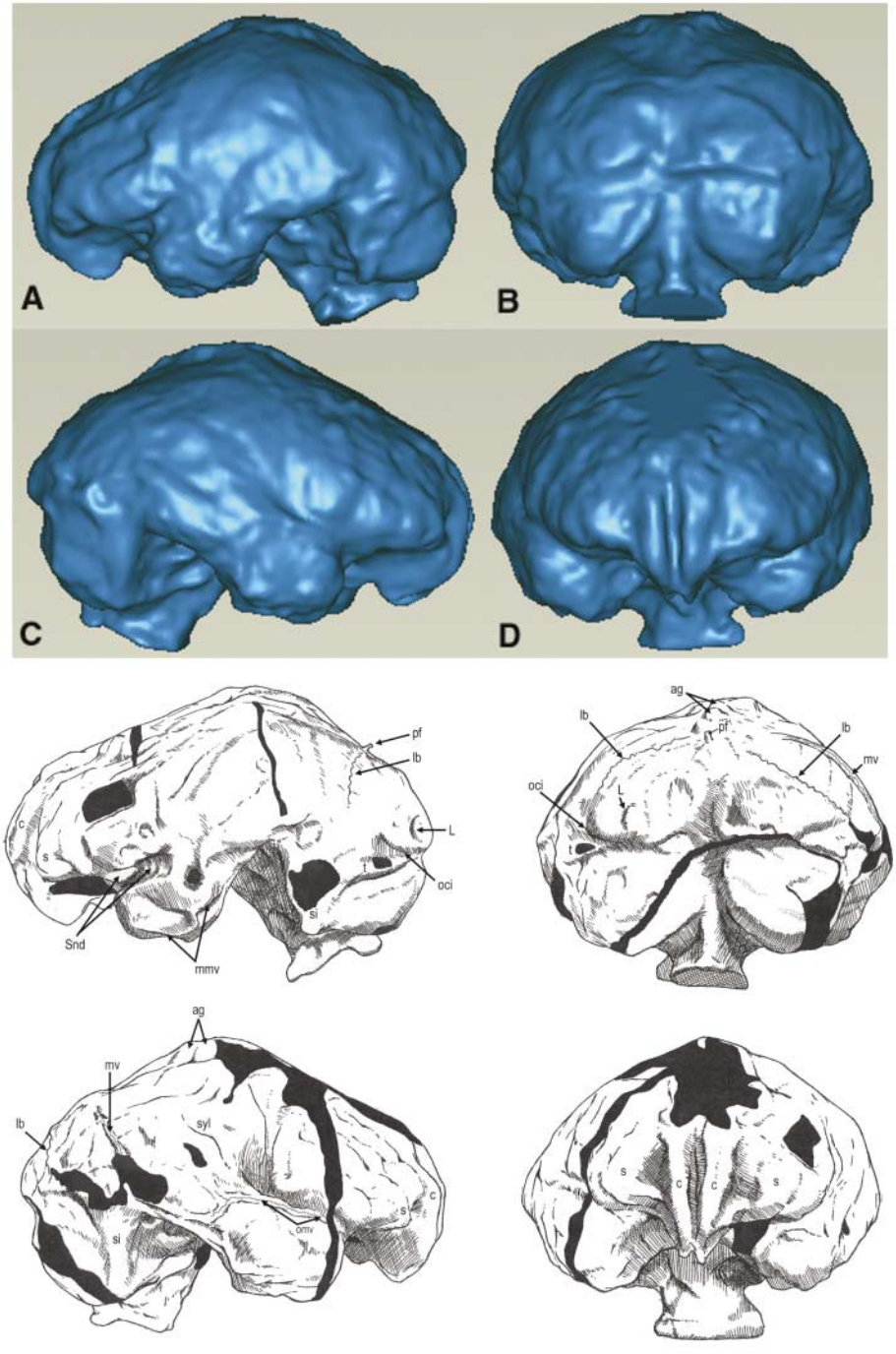

Fig. 3. Virtual endocast of LB1 (top). Views: (**A**), left lateral; (**B**), posterior; (**C**), right lateral; (**D**), frontal. Identifications of features are shown on corresponding sketches (bottom) (damaged areas are blackened) as follows: ag, arachnoid granulations; c, frontal lobe convolutions; lb, lambdoid suture; L, lunate sulcus; mv, meningeal vessels; mmv, middle meningeal vessels; oci, inferior occipital sulcus; omv, orbital meningeal vessels; pf, foramen for parietal emissary vein; s, frontal lobe swelling; si, sigmoid sinus; Snd, Sylvian notch and depression; Syl, Sylvian fissure; t, transverse sinus.

The lambdoid suture is located more rostrally on the left than on the right side of the endocast (Fig. 3). Both the skull and the endocast show a left frontal and right occipital petalia (Fig. 1A) that, in humans, are statistically correlated to some degree with left-handedness (*20*). After entering the middle cranial fossa, small anterior branches of the middle meningeal vessels course rostrally across the ventral surface of the right temporal lobe and across the ventrolateral surface on the left. On the right, a branch from another meningeal vessel enters the middle braincase from the orbital region and courses caudally across the temporal lobe inferior to the Sylvian fissure. Similar orbital contributions are common in apes and have been reported for certain *H. erectus* endocasts by some workers (*21*) but not others, who used a scoring system for modern humans (*22*). Traces of meningeal vessels are also reproduced in the right parietal region, and several arachnoid granulations appear near the vertex on the right. LB1 reproduces somewhat (artifactually) distorted transverse and sigmoid sinuses. A cast of the parietal emissary foramen appears near the medial end of the left lambdoid suture.

The right side of LB1's endocast reproduces part of the Sylvian fissure and numerous small sulci on the lateral temporal and dorsolateral frontal lobes (Fig. 3). The right orbital surface reveals three small sulci that do not extend onto the dorsal surface (the left orbital surface is damaged). In the left occipital region, LB1 reproduces an inferior occipital sulcus and a small crescent-shaped lunate sulcus medial to it and caudal to the lambdoid suture. The position of the lunate sulcus is derived and suggests cortical reorganization in the posterior parietal association cortex as compared with apes (*2*, *23*).

LB1's orbital caps are not delimited rostrally by apelike orbitofrontal sulci that incise the borders and course toward the temporal poles on the orbital surfaces (*23*, *24*). Instead, LB1's gyrification, orientation, and relation-

ship of the lateral prefrontal cortex relative to the temporal poles appear derived. Following Connolly (*23*), we decline to identify rami that border the human pars triangularis (part of Broca's area) on the left, although the general morphology in this region would be consistent with their existence. On the left (and to a lesser extent the right), a distinct Sylvian notch separates the temporal from the frontal lobe and continues caudally as a depression. This region corresponds to a Sylvian crest within the skull of LB1 that, in humans, sometimes occurs in particularly thick skulls and is correlated with Sylvian depressions on endocasts, although the brains are, if anything, more opercularized in the corresponding area (*23*).

The depression for the superior sagittal sinus on LB1's frontal lobes is bordered laterally by large convolutions [which probably contained additional furrows not reproduced on the endocast (*23*)] that curve around the rostral tip of the endocast onto the orbital surface and meet at the foramen caecum. Dimples separate these convolutions laterally from swellings that square off the frontal lobes and give their outline a ruffled appearance in dorsal view (Fig. 1A). Although hints of such contours may be seen in chimpanzee and hominin endocasts such as in the no. 2 specimen from Sterkfontein (*9*), the extent of these expansions in the frontal polar region of LB1 is unusual. This part of the prefrontal cortex in humans and apes consists of Brodmann's area 10, which in humans may be involved in higher cognitive processes such as the undertaking of initiatives and the planning of future activities (*25*). Human frontal lobes are not larger than expected for apes of similar brain volume (*26*), but area 10 is both absolutely and relatively enlarged in *H. sapiens* as compared with apes (*25*). LB1's polar convolutions appear derived compared with those of *H. erectus* and other early hominins. Unlike the frontal lobes, human temporal lobes appear to be somewhat larger than expected for an ape brain of human size (*26–28*); thus, LB1's extremely wide temporal lobes (brachycephaly; fig. S3) may represent another derived feature.

Our data show that LB1's well-convoluted brain could not have been a miniaturized version of the brain of either *H. sapiens* or *H. erectus*. Nevertheless, its similarities with *H. erectus* strongly suggest a phylogenetic connection, although its australopithecine-like brain/body size ratio and morphology of the femur and pelvis (*29*) are not expected in a miniaturized descendant of a larger-bodied *H. erectus* (which, instead, would be expected to scale allometrically along the ontogenetic curve predicted for *H. erectus*) (fig. S1). Although it is possible that *H. floresiensis* represented an endemic island dwarf that, over time, became subject to unusual allometric constraints, an alternative hypothesis is that *H. erectus* and *H. floresiensis* may have shared a common ancestor that was an unknown small-bodied and small-brained hominin (*1*).

References and Notes

1. P. Brown *et al.*, *Nature* **431**, 1055 (2004).
2. R. L. Holloway, D. C. Broadfield, M. S. Yuan, *The Human Fossil Record, Volume Three, Brain Endocasts–The Paleoneurological Evidence* (Wiley-Liss, Hoboken, NJ, 2004).
3. M. J. Morwood *et al.*, *Nature* **431**, 1087 (2004).
4. M. Henneberg, A. Thorne, *Before Farming* (online journal) **4**, article 2 (2004).
5. G. C. Conroy, M. W. Vannier, in *Hominid Evolution: Past, Present and Future*, P. V. Tobias, Ed. (Liss, New York, 1985), pp. 419–426.
6. G. C. Conroy, M. Vannier, P. V. Tobias, *Science* **247**, 838 (1990).
7. G. C. Conroy *et al.*, *Science* **280**, 1730 (1998).
8. F. Spoor, N. Jeffery, F. Zonneveld, *J. Anat.* **197**, 61 (2000).
9. Falk *et al.*, *J. Hum. Evol.* **38**, 695 (2000).
10. The CT-estimated cranial capacity was 417 cm^3, as opposed to 380 cm^3 measured with mustard seeds (*1*). The 37-cm^3 difference is attributable to variation in how cranial holes were plugged and thus to measurement error associated with the current reconstructions.
11. A. Verloes, *Orphanet Encyclopedia*, www.orpha.net/data/patho/GB/uk-MVMSG.pdf (February 2004).
12. A. Kumar *et al.*, *J. Biosci.* **27**, 629 (2002).
13. W. H. Flower, *J. Anthropol. Inst. G. B. Ireland* **18**, 3 (1889).
14. L. L. Cavalli-Sforza, in *African Pygmies*, L. L. Cavalli-Sforza, Ed. (Academic Press, New York, 1986), pp. 81–93.
15. B. T. Shea, R. C. Bailey, *Am. J. Phys. Anthropol.* **100**, 311 (1996).
16. R. Passingham, *New Scientist* **27**, 510 (1975).
17. A. H. Schultz, *Primatologica* **I**, 887 (1956).
18. H. Jerison, *Evolution of the Brain and Intelligence* (Academic Press, New York, 1973).
19. J. Diamond, *Science* **306**, 2047 (2004).
20. M. LeMay, *Am. J. Neuroradiol.* **13**, 493 (1992).
21. D. Falk, *Am. J. Phys. Anthropol.* **92**, 81 (1993).
22. F. Weidenreich, *Palaeontol. Sinica New Ser. D.* **3**, 1 (1938).
23. C. J. Connolly, *External Morphology of the Primate Brain* (Thomas, Springfield, IL, 1950).
24. D. Falk, *Science* **221**, 1072 (1983).
25. K. Semendeferi *et al.*, *Am. J. Phys. Anthropol.* **114**, 224 (2001).
26. K. Semendeferi, in *Evolutionary Anatomy of the Primate Cerebral Cortex*, D. Falk, K. R. Gibson, Eds. (Cambridge Univ. Press, Cambridge, 2001), pp. 257–289.
27. K. Semendeferi, H. Damasio, *J. Hum. Evol.* **38**, 317 (2000).
28. J. K. Rilling, R. A. Seligman, *J. Hum. Evol.* **42**, 505 (2002).
29. C. Groves, *Before Farming* (online journal) **4**, article 1 (2004).

30. We thank the National Geographic Society (grant 7760-04) and D. Hamlin for helping to bring this research to fruition. X. Wu of the Institute of Vertebrate Paleontology and Paleoanthropology, Chinese Academy of Sciences, provided the measurements for *H. sapiens* in Table 1; K. Mowbray of the American Museum of Natural History provided the cast of the microcephalic skull and pygmy skull; and B. Latimer and L. Jellema of the Cleveland Museum of Natural History loaned additional skeletal material. We appreciate T. Gebke and C. Tinscher's technical assistance in CT scanning, B. Macy's production of physical endocasts, B. Worthington's illustrations of LB1's endocast (Fig. 3), and E. Chambless's help with manuscript preparation.

Supporting Online Material

www.sciencemag.org/cgi/content/full/1109727/DC1
Materials and Methods
SOM Text
Figs. S1 to S5
Tables S1 to S3
References

13 January 2005; accepted 11 February 2005
Published online 3 March 2005;
10.1126/science.1109727
Include this information when citing this paper.

Vasopressin and Oxytocin Excite Distinct Neuronal Populations in the Central Amygdala

Daniel Huber,[1] Pierre Veinante,[2] Ron Stoop[1]*

Vasopressin and oxytocin strongly modulate autonomic fear responses, through mechanisms that are still unclear. We describe how these neuropeptides excite distinct neuronal populations in the central amygdala, which provides the major output of the amygdaloid complex to the autonomic nervous system. We identified these two neuronal populations as part of an inhibitory network, through which vasopressin and oxytocin modulate the integration of excitatory information from the basolateral amygdala and cerebral cortex in opposite manners. Through this network, the expression and endogenous activation of vasopressin and oxytocin receptors may regulate the autonomic expression of fear.

The amygdala plays an important role in anxiety and fear behavior. Fear learning involves its lateral and basolateral parts, where the association between incoming fearful and neutral stimuli leads to potentiation of synaptic transmission. These parts project to the central amygdala (CeA), whose efferents to the hypothalamus and brainstem trigger the autonomic expression of fear (*1*). Selective gating of synaptic transmission through the CeA could therefore modulate the fear response (*2*, *3*). Indeed, recent studies suggest that increased inhibition within the CeA could underlie the anxiolytic effects of benzodiaze-

[1]Department of Cellular Biology and Morphology and Centre for Psychiatric Neuroscience, Department of Psychiatry, Centre Hospitalier Universitaire Vaudois, University of Lausanne, Switzerland. [2]Neurophysiologie Cellulaire et Intégrée, Unité Mixte de Recherche 7519, CNRS, Université Louis Pasteur, Strasbourg, France.

*To whom correspondence should be addressed. E-mail: rstoop@unil.ch

Supporting Online Material

Materials and methods

CT scans of the LB1 were performed, using a Siemens Emotion CT scanner (Siemens Medical Systems,Inc., Erlangen, Germany), in Jakarta Selatan, Indonesia. Parameters included a 512x512 matrix, 2mm collimation, 1mm reconstruction interval, and a H70s reconstruction kernel. CT image data of the LB1 were received in DICOM format at Washington University School of Medicine. The CT scan parameters (and reconstruction kernel) used at Washington University for the comparison material were chosen to produce optimal reconstructions. Our material was scanned with a Siemens Sensation 64 (Siemens Medical Systems, Erlangen, Germany) clinical multi-slice, computed-tomography (MCT) scanner, located in Barnes Jewish Hospital (St. Louis, MO, USA). Specimens were aligned along a cranial-caudal axis with the nose facing upward, to simulate a normal anatomical head orientation. Scanning parameters included a 512 x 512 matrix, 120kVp, 300 effective mAs, 32 detectors with dual sampling to achieve a 0.6mm collimation, 1 second table increment per gantry rotation, pitch of 0.8, reconstruction interval of 0.5mm, and a H50s reconstruction kernel. The "very sharp" reconstruction kernel used for LB1 may have introduced artifacts. With the higher-depth-resolution images that we used, a high-sharpness kernel was unnecessary. For LB1, the slice thickness was 1 mm, and the in-plane resolution < 0.4 mm. Because the features that we identified crossed many planes, our ability to visualize the features was not compromised by the Nyquist frequency (*S1*), which dictates the resolution above which a feature must be sampled to fully reconstruct the feature. The CT resolution for LB1 was fully adequate for the purposes of our study. All data were archived to compact disk in DICOM format and transferred to a standalone workstation for processing. Using commercially available software packages, Mimics 8.11, (Materialise, Inc., Ann Arbor, MI, USA), and Analyze 6.1, (Biomedical Imaging Resource, Mayo Clinic, Rochester, MN, USA), the CT image data were visualized assessed and inspected for artifacts and damaged areas.

Virtual endocasts were made using Mimics 8.11 software. This software provides tools to convert grayscale CT image data into a wireframe "virtual" model. First, the skull is segmented (isolated) from surrounding air and labeled using a combination of global and local thresholding operations together with a region growing operation. The internal braincase was enclosed, using manual segmentation, to close any contour gaps in the skull, such as at the eye sockets, and also to "fill" any damaged areas in LB1's skull. Once the internal braincase was fully enclosed, as would be done making a traditional latex endocast, the virtual endocast object was defined with a cavity fill operation and a 3D object was created within the Mimics 3D Object module. This was done using the high quality option. By means of the edge extraction tools within the Mimics STL module, a triangulated surface definition was created from the endocast 3D object.

Using direct manufacturing technology, physical endocasts of LB1, the pygmy, and the microcephalic were produced from the virtual endocast data with a process known as fused deposition modeling (Dimension FDM, Stratasys, Inc, Rochester, MN, USA). The virtual endocast models were processed and converted to compatabile direct manufacture format by REALADI (St. Charles, MO, USA) for subsequent fabrication of the physical endocasts by QTE (St. Charles, MO). Shape comparisons were performed between the LB1 virtual endocast and endocasts generated from the other specimens by means of Geomagic Studio 5 software (Raindrop Geomagic, Inc., Research

Triangle Park, NC, USA) to normalizie the virtual endocasts to the volume of the LB1 endocast. Geomagic Studio 5 was also used to measure the virtual endocast of LB1.

Whether or not they are produced artifically or virtually, endocasts reproduce details of external brain morphology that were imprinted in braincases. These details may be interpreted by referring to analyses that compare sulcal patterns on endocasts with *corresponding* brains and used to interpret endocast morphology of fossil hominins and the comparative cortical anatomy of living primates (*S2*). Because of documentation about the difficulty of accurately identifying small sulci on endocasts (*S2*), we declined to name the numerous small sulci that are reproduced on LB1's endocast (e.g., on the right frontal lobe, and the anterior rami of the Sylvian fissure). We did, however, identify large sutures, vessels, gyri, a lunate sulcus, and part of the Sylvian fissure on the endocast (Fig. 3). This was done using a transparent 3DCT-generated replica of LB1's skull, a rubber endocast prepared from that replica, and a virtual endocast and solid model of the virtual endocast that were prepared *after* the original CT data were rendered (in St. Louis) to maximize details of the internal braincase. All four sources were extremely useful. After tentative identifications were made (by Falk), Falk and Smith went through the CT data (physical endocasts and skull replica in hand) to verify or exclude as possible artifact every feature. Features in the blackened areas on the sketches in fig. 3 were questionable.

Text

Microcephalia vera (*MV*, primary or true microcephaly) is an autosomal recessive pattern associated with eight loci and three known genes. *MV* is characterized by small cranial vaults relative to facial skeletons, sloping foreheads and pointed vertices (*S3*-*S4*). The virtual endocast that we produced from a cast of an *MV* skull reflects the pathological shape of the skull. Microcephaly with simplified gyral pattern (*MSG*) is another form of congenital microcephaly, with five recognized types manifesting reduced numbers and shallowness of cortical sulci (*S5*). The cortical topography of LB1's endocast precludes it from this form of microcephaly. Secondary microcephaly is a catch-all diagnosis for individuals with occipitofrontal circumferences below -2 standard deviations for age and sex (*S3*), and is not necessarily associated with a pointed head (if it were, it would automatically be ruled out for LB1). Unlike *MV*, secondary microcephaly may be attributed to various causes including toxic intrauterine exposure, chromosomal anomalies, or infectious diseases (*S3*). Since LB1 lacks the diagnostic head shape associated with *MV* and lacks the gyral morphology associated with *MSG*, its interpretation as a microcephalic can only be made by claiming that it is a secondary microcephalic (*S6*). This amounts to saying LB1 is small-headed (literally microcephalic) because it is small-headed, which does not lend itself to hypothesis testing.

Relative brain size (RBS) is confounded by allometric scaling constraints that apply ontogenetically as individuals develop from small-bodied babies to adults (*S7*) and in interspecific comparisons of small-bodied with larger-bodied primates (*S8*). Humans and chimpanzees have similar trajectories for brain growth, but the high rate of human postnatal brain growth shifts the human curve above that of *Pan* (fig. S1, A). This is why humans have brains that are approximately three times as large as expected for apes of the same body size (*S7*, S9-*S11*),

a widely known relationship that may simply be expressed as an index of RBS equal to 3 (i = 3) (fig. S1, B). By this convention, i = 1 for apes.

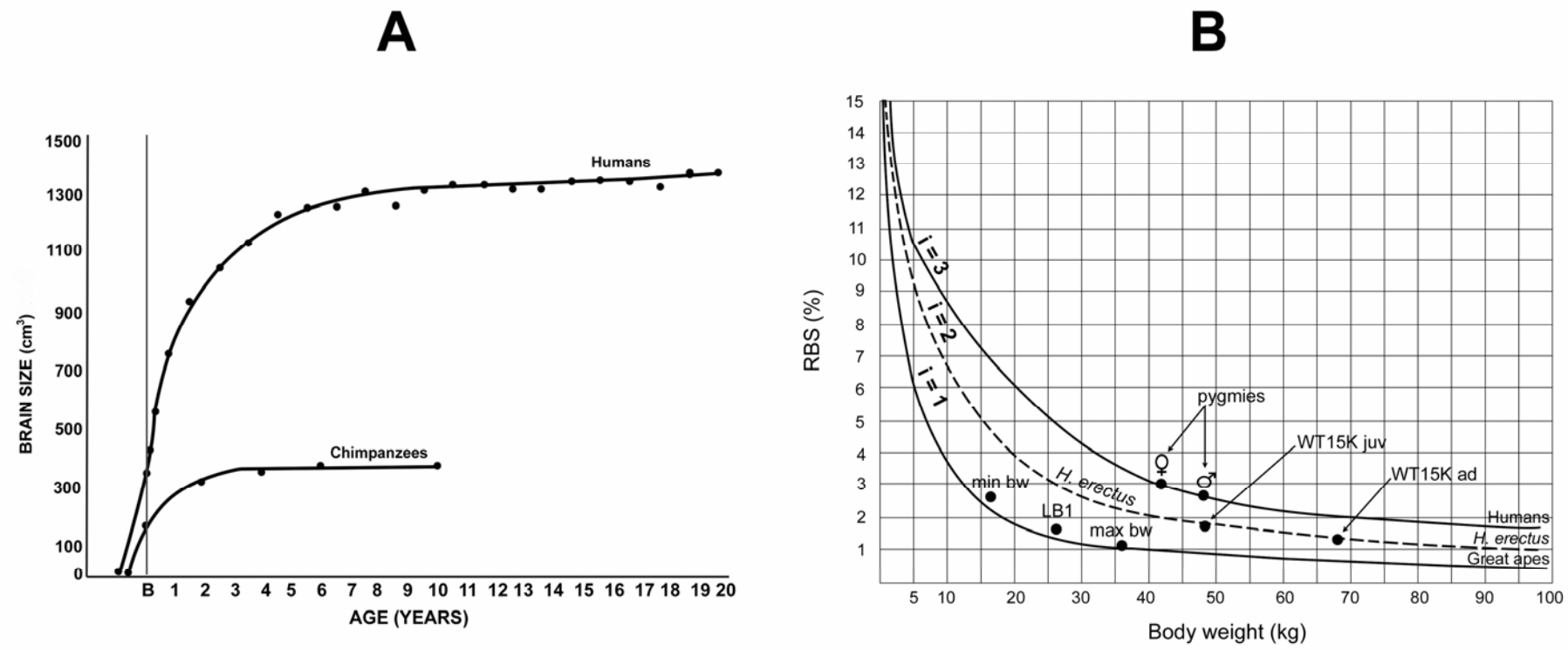

Fig. S1. **A**, Ontogenetic brain growth curves for humans and chimpanzees, B = birth (*S7*); **B**, Cranial capacity in cm^3 as percentage of body weight in g (RBS, relative brain size) plotted against body weight (kg) for humans and apes (*S8*). Indices describe ape-like RBS (i=1) and RBS that are twice (i=2) and three times (i=3) those expected for apes of equivalent body weights. Pygmies are placed on the human curve at their mean body weights of 42 kg and 48 kg for 319 women and 405 men (Congo) (*S12*). The curve for *H. erectus* is hypothetical because it is based on data showing that i = 2 from only one available skeleton (KNM-WT 15000). Estimated juvenile and adult weights for WT 15000 are 48 and 68 kg and juvenile and adult cranial capacities are 880 and 909 cm^3 (*S13*); LB1's cranial capacity of 417 cm^3 places it on or near the ape curve at its minimum, mean, and maximum body weight estimates (16-36 kg, mean = 26 kg) (*S14*).

The ontogenetic decrease in RBS for humans and great apes is shown in fig. S1, B. Again, the shapes of the curves are similar, but with humans coursing above apes. This allometric scaling explains why infant humans and chimpanzees (and other primates) appear to have such relatively big heads (brains) compared with adults despite their absolute brain sizes being smaller. The human curve in B also illustrates why human pygmies appear to have relative large heads (*S15*), i.e., they are scaling along the human ontogenetic curve (*S16*), but at lower body weights and therefore larger RBS.

Encephalization quotients (EQs) for fossil hominins must be viewed cautiously because (among other reasons), without associated skulls, it is difficult to attribute species to postcrania such as femurs that are used to predict body mass or stature. Conservatively, for *Homo erectus* we must rely on the one relatively complete skeleton in the fossil record, namely ~1.5 ma KNM-WT 15000 from Nariokotome, Kenya. By the time he reached adulthood, it was projected that this 'lad' would have reached a stature of over six feet and a cranial capacity of 909 cm^3 (*S13*). That capacity is twice the means for both *A. africanus* and *Paranthropus* (451 and 450 cm^3) (*S17*), and roughly twice the means for living great apes (490 cm^3 for gorillas, 375 cm^3 for common chimpanzees and for orangutans [*S18*]). It is also 2/3 of 1364 cm^3, which is very close to the oft-cited world mean for contemporary *Homo sa*piens of 1350 cm^3. Therefore, the best guess that can be made with these limited data is that African *H. erectus* that lived ~1.5 ma had a brain mass that was twice the size predicted for nonhuman primates of equivalent body mass (i = 2) or, put another way, *H. erectus* was two-thirds as encephalized as *H. sapiens*. Fast-forwarding to ~0.9 ma in Java, the Trinil 2 endocast (Table 1) has a cranial capacity of 940 cm^3 (*S19*). Although this specimen lacks an associated skeleton, its shape resembles the *Homo erec*tus endocasts from China and its cranial capacity is not much larger than that of WT 15000's, which would be consistent with its being positioned on the hypothetical curve for *Homo erectus* in fig. S1, B.

One would expect RBS of a 'miniaturized' *Homo erectus* population to scale as it does for miniaturized *Homo sapiens* populations (pygmies) – namely along its (ancestral) species' ontogenetic curve. That means that the miniaturized *Homo erectus* specimens should approximate a RBS index of i = 2, which LB1's does not. Rather, LB1 has an ape-sized body and an ape-sized brain, or i = 1. (Certain cranial capacity estimates for early hominins are smaller than previously believed [*S17, S20, S21*], which is consistent with i = 1 for australopithecines.)

Figures and legends

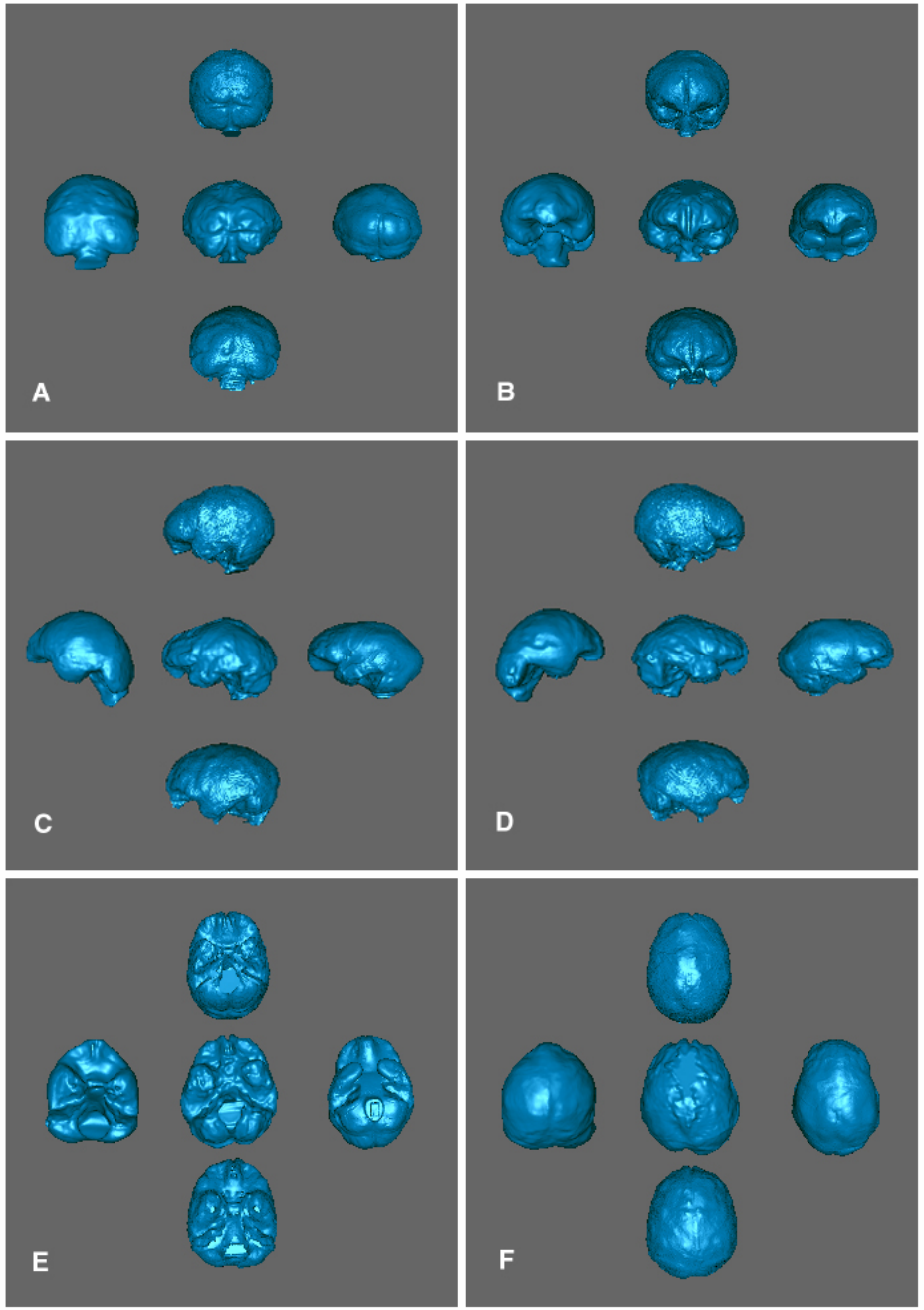

Fig. S2. Comparisons of virtual endocasts of LB1 (center), *Homo sapiens* (top), chimpanzee (bottom), a human microcephalic (left) and *Homo erectus* (right). Views are A, posterior; B, frontal; C, left lateral; D, right lateral; E, inferior; F, dorsal.

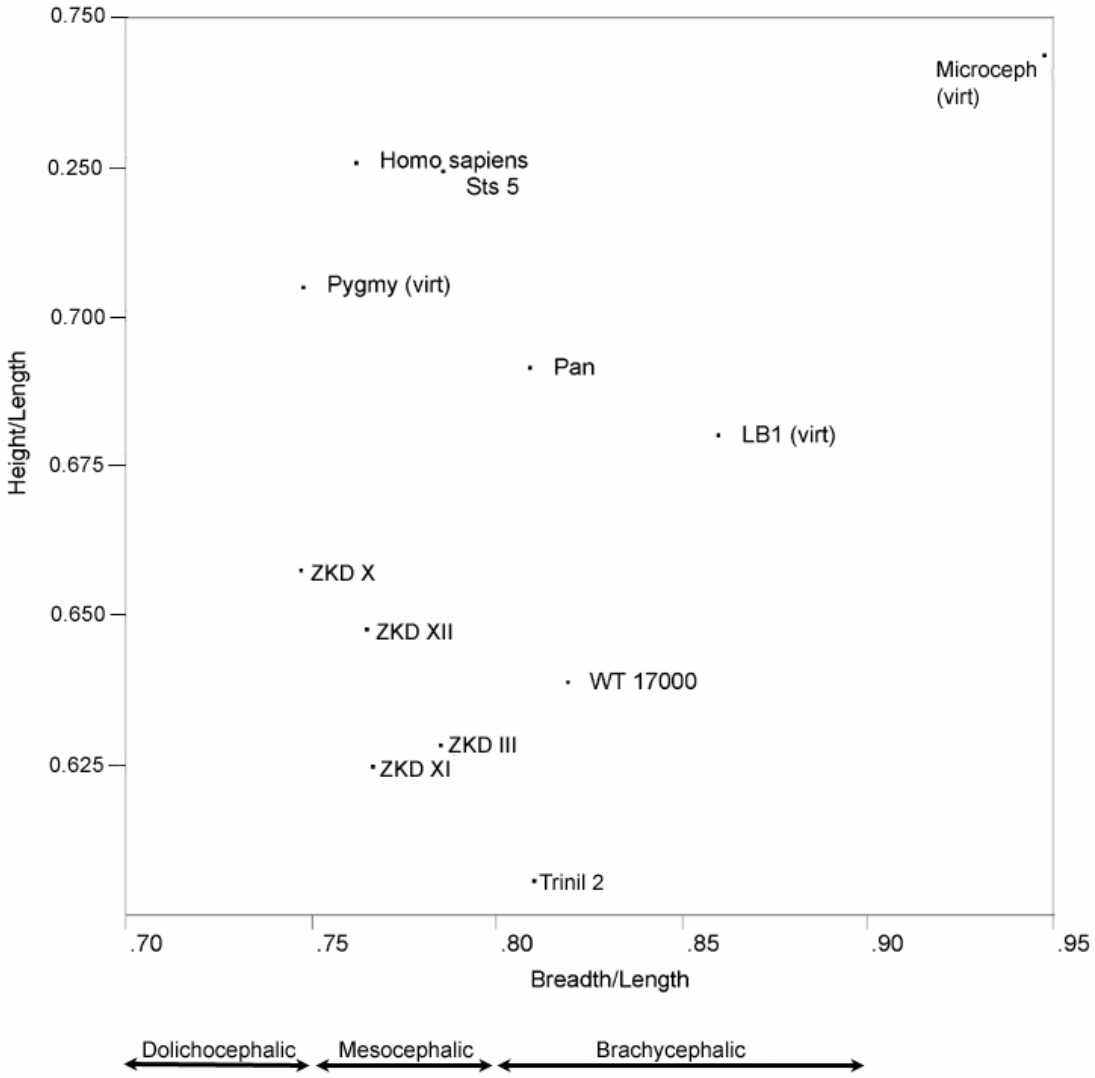

Fig. S3A. Height/length plotted against breadth/length. Virt = virtual (computer model).

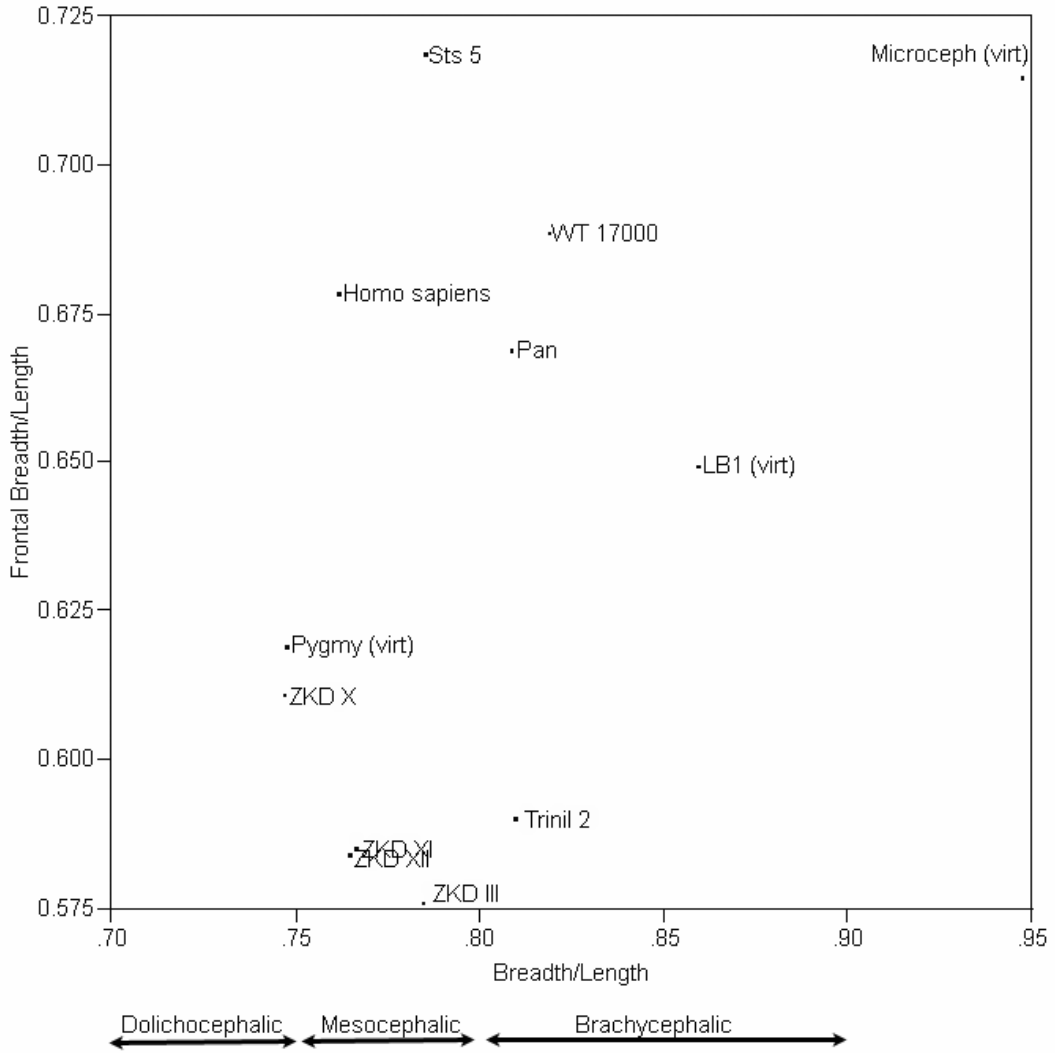

Fig. S3B. Frontal breadth/length plotted against breath/length. Virt = virtual (computer model).

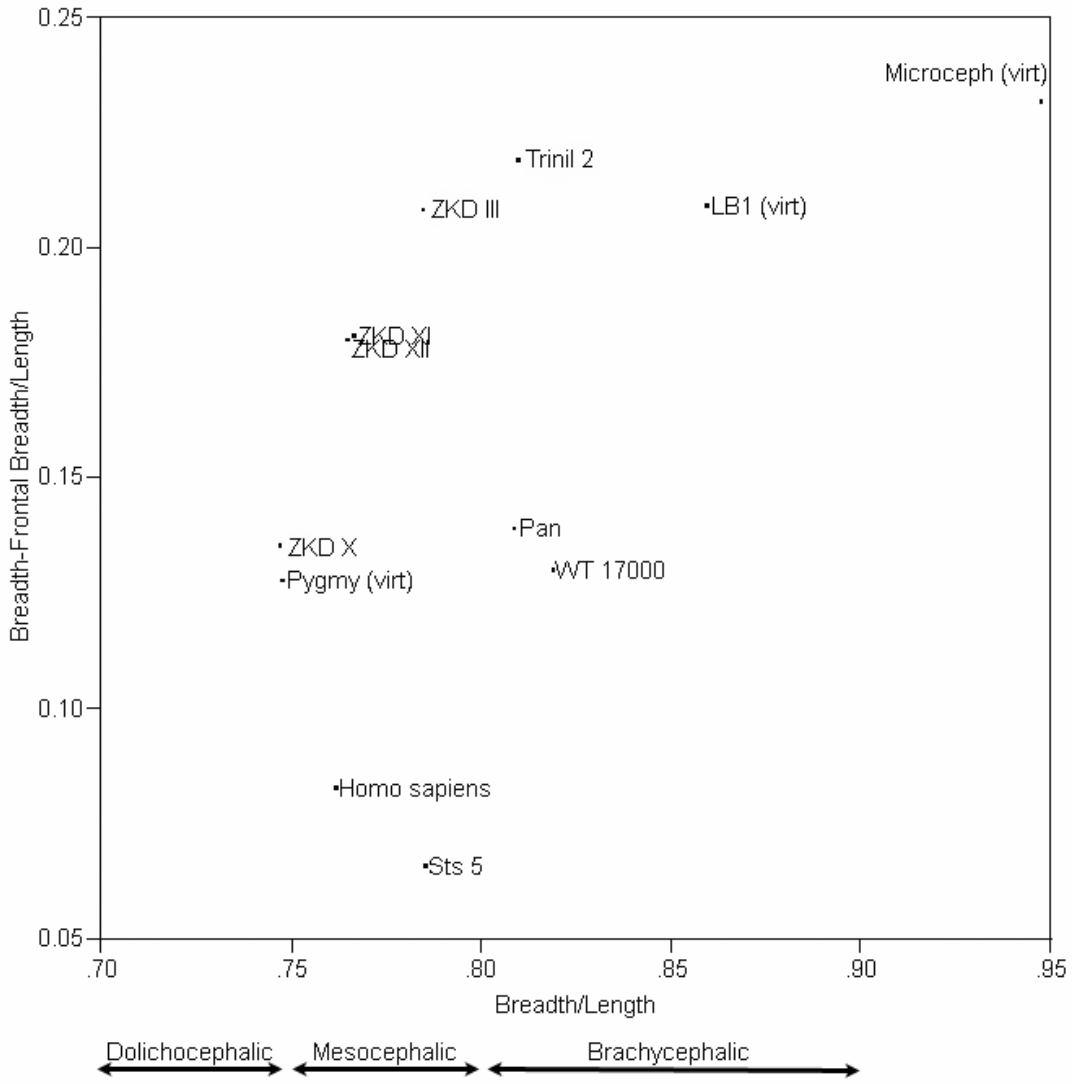

Fig. S3C. Breadth minus frontal breadth/length plotted against breadth/length. Virt = virtual (computer model).

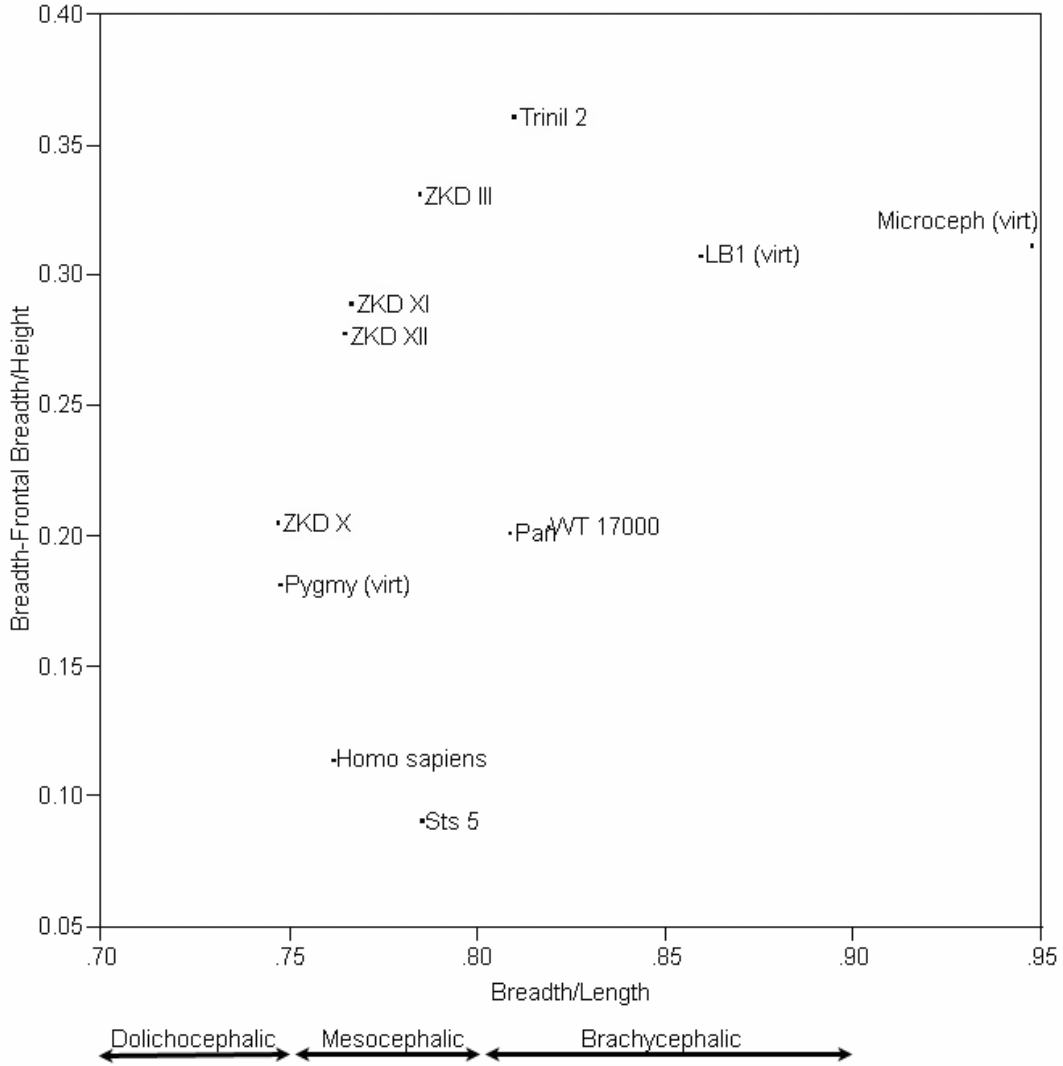

Fig. S3D. Breadth minus frontal breadth/length plotted against height. Virt = virtual (computer model).

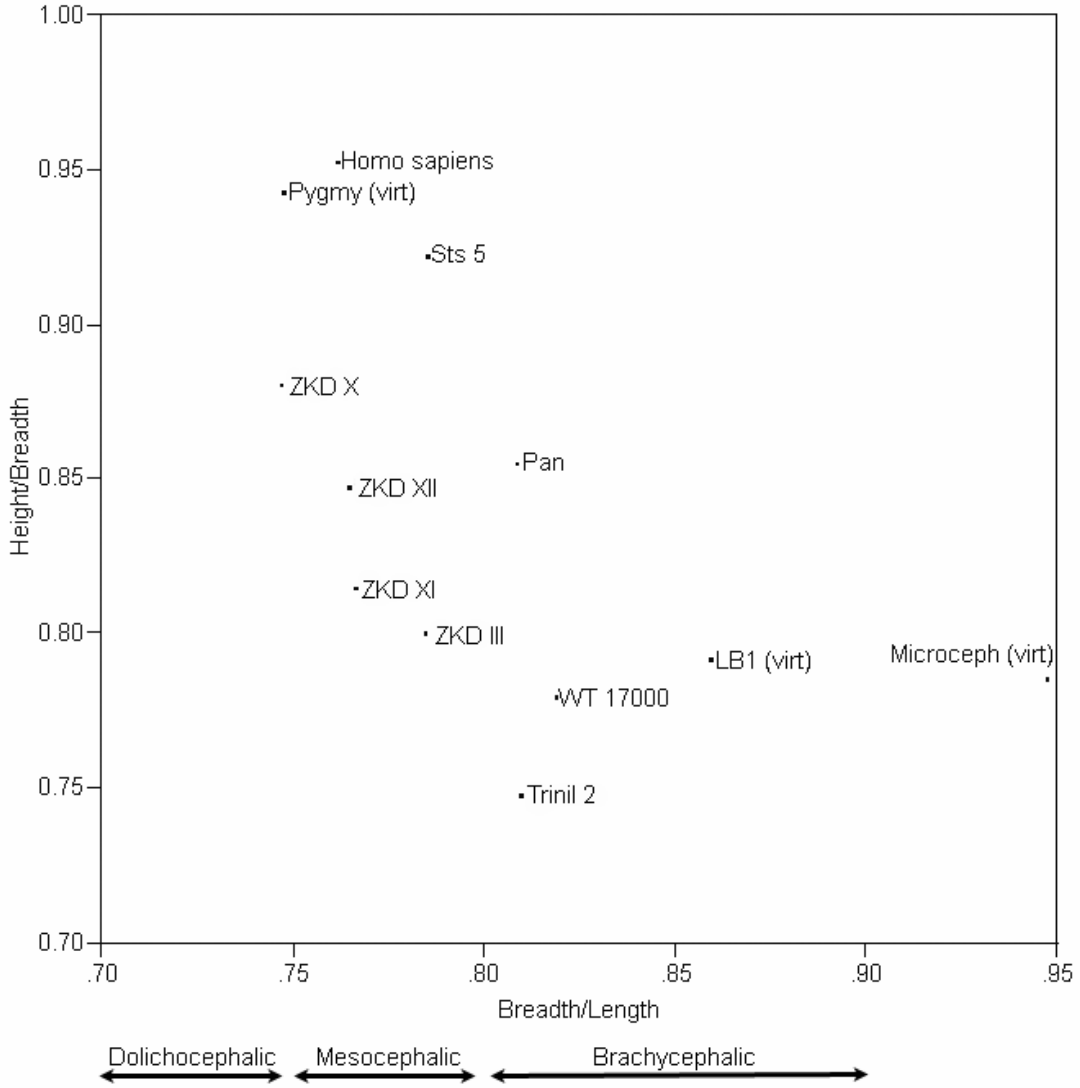

Fig. S3E. Height/breadth plotted against breadth/length. Virt = virtual (computer model).

Fig. S3 (A-E). Bivariate plots for five of the ratios listed in Table 1 against breadth/length (the cephalic index). These plots confirm that LB1 generally resembles *Homo erectus*, although it is more brachycephalic. Compared with *Homo erectus*, the endocast of LB1 is also relatively taller compared with length (S3A) and wider in front (S3B). Narrowing of the width of the frontal lobe compared with the width of the

temporal lobe groups LB1 with *Homo erectus* (S3C, S3D) as does its height relative to breadth (S3E). These plots also confirm that the microcephalic is an outlier, and that the pygmy tends to resemble other *Homo sapiens*. Sts5 (*Australopithecus africanus*) shares shape features with *Homo sapiens* (*S17*), while KNM-WT 17000 (*Paranthropus aethiopicus*) is frequently near *Pan*.

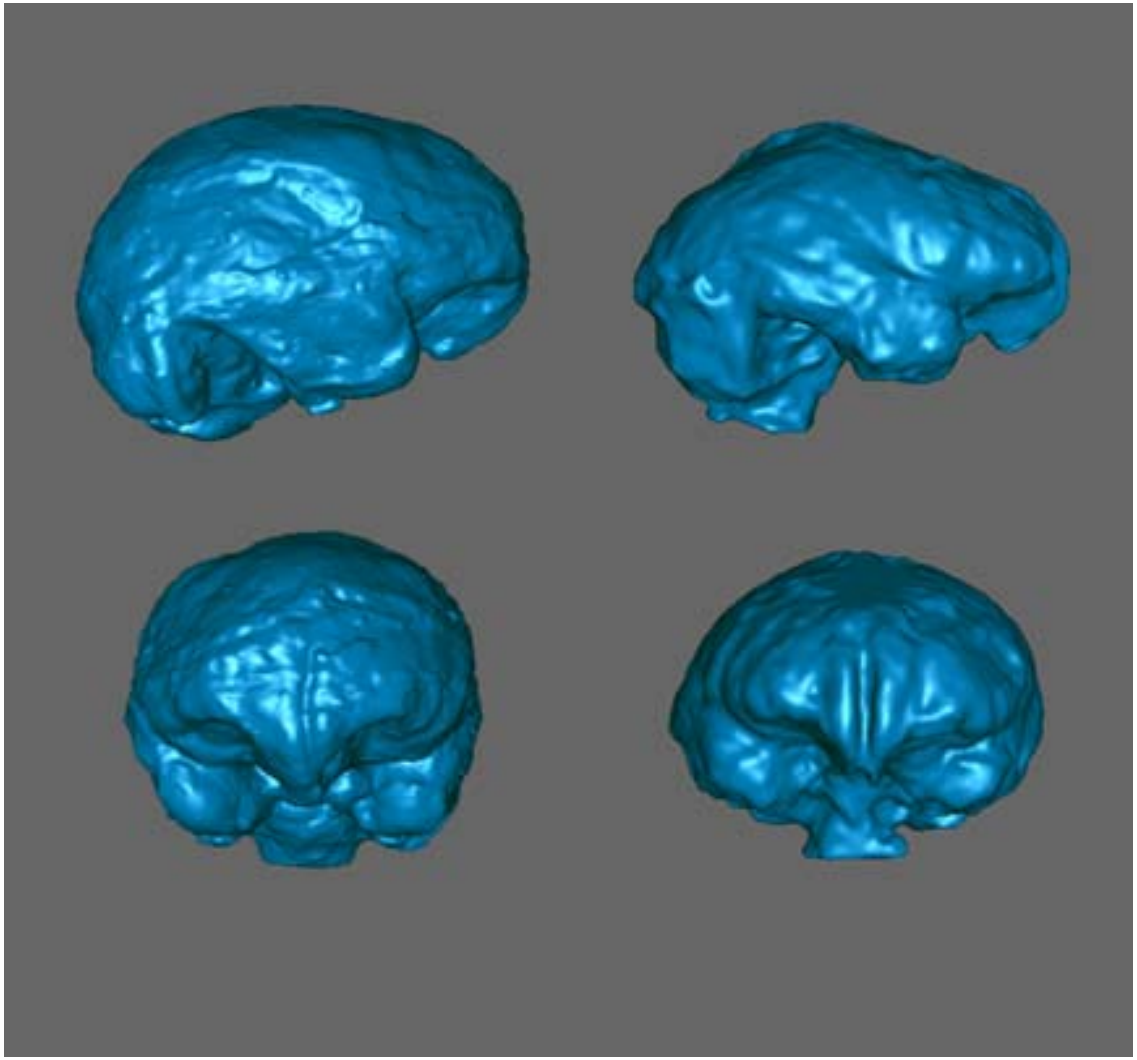

Fig. S4. Virtual endocasts of Sts 5 (*Australopithecus africanus*), left; LB1, right. Above, right lateral views; Below, frontal views.

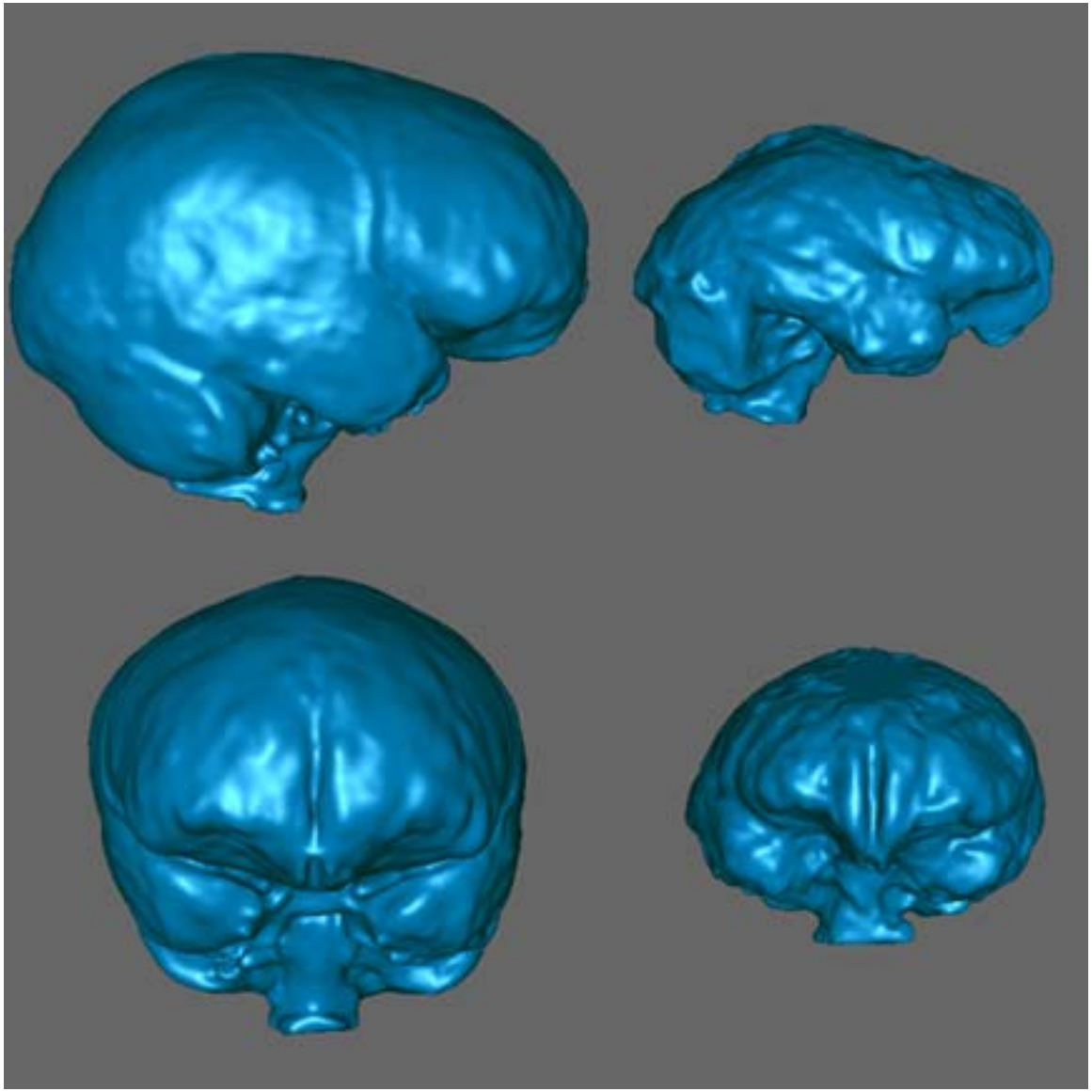

Fig. S5. Virtual endocasts of human pygmy, left; LB1, right. Above, right lateral views; Below, frontal views.

Tables and legends

Table S1. Reliability of *Homo erectus* endocast measurements.

	Length		Breadth		Height		Frontal Breadth	
	Mean Δ* (± Std Dev)†	Percent Δ (± Std Dev)	Mean Δ (± Std Dev)	Percent Δ (± Std Dev)	Mean Δ (± Std Dev)	Percent Δ (± Std Dev)	Mean Δ (± Std Dev)	Percent Δ (± Std Dev)
Homo erectus (ZKD III, ZKD X, ZKD XI, ZKD XII, Trinil 2)	.048 (1.0)	(<0.01) (<0.01)	0.34 (1.7)	<0.01 (0.01)	2.04 (.86)	0.02 (<0.01)	0.9 (1.28)	<0.01 (0.01)

*Difference in mm or percent. †Standard deviation in mm or percent.

Table S2. Basal-view endocast measurements (mm) and indices for *Gorilla*, *Pan*, *Homo*, WT 17000, Sts 5, and LB1. All values except for LB1 taken from *S17*.

	bat-bat [1]	mat-mat [2]	mbat-rof(tan) [3]	cob-rof (tan) [4]	rob-rof (tan) [5]	rof(tan)-bpc(tan) [6]	Cranial capacity (cm3) [7]	Length mbat-cob (3-4) [8]	Length olf bulb (4-5) [9]	base-caudal to bat (6-3) [10]	1/6	2/6	3/6	4/6	5/6	(3-4)/6	(4-5)/6	(6-3)/6
Gorilla (mean) (n = 10)	49	77.6	34	16.6	4.6	120.9	483.5	17.4	12	86.9	0.41	0.64	0.28	0.14	0.04	0.14	0.10	0.72
Pan (mean) (n = 18)	47.3	74.94	31.41	16.44	4.79	107.56	392.67	14.76	11.26	76.33	0.44	0.70	0.29	0.15	0.04	0.14	0.11	0.71
Homo (mean) (n = 10)	69.7	108.9	38.9	30.3	9	150.1	1350	8.6	21.3	111.2	0.46	0.73	0.26	0.20	0.06	0.06	0.14	0.74
WT 17000	50	74	34	20	7	114	410	14	13	80	0.44	0.65	0.30	0.18	0.06	0.12	0.11	0.70
Sts 5	56	85	39	30	14	118	485	9	16	79	0.47	0.72	0.33	0.25	0.12	0.08	0.14	0.67
LB1 (virtual)*	57.8	78.9	29.4	22	10	114.1	417	7.4	12	84.7	0.51	0.69	0.26	0.19	0.09	0.06	0.11	0.74

*Computer model

Table S3. Principal Components resulting from the analyses of indices in Tables 1 and Table S2.

Principal Components (see Table 1, Fig. 2A)

Eigenvalue	2.6500	1.9675	0.3821	0.0004
Percent	53.0002	39.3509	7.6419	0.0070
Cum Percent	53.0002	92.3511	99.9930	100.0000
Eigenvectors				
B/L	-0.15673	0.68886	0.05586	0.36755
H/L	0.47975	0.37803	0.53355	-0.58503
FB/L	0.38864	0.50829	-0.48906	0.20113
B-FB/L	-0.54460	0.23004	0.53629	0.19114
H/B	0.54556	-0.26699	0.43060	0.66758

Principal Components (see Table S2, Fig. 2B)

Eigenvalue	4.5251	2.4024	0.7803	0.2583	0.0339	0.0000	0.0000	-0.0000
Percent	56.5632	30.0304	9.7542	3.2288	0.4233	0.0000	0.0000	-0.0000
Cum Percent	56.5632	86.5936	96.3479	99.5767	100.0000	100.0000	100.0000	100.0000
Eigenvectors								
1/6	0.37048	-0.26483	-0.47065	0.28486	0.69996	0.00000	0.00000	0.00000
2/6	0.39181	-0.12394	0.38024	0.76794	-0.31113	-0.00000	-0.00000	-0.00000
3/6	0.11356	0.62486	-0.02334	0.10261	0.11885	0.42375	0.61652	-0.10860
4/6	0.45742	0.12239	-0.04252	-0.24336	-0.12535	-0.73210	0.38135	0.13285
5/6	0.41556	0.15445	-0.44021	-0.13262	-0.40353	0.34786	-0.30756	0.46222
(3-4)/6	-0.40533	0.30691	0.02874	0.32956	0.21586	-0.23905	-0.03962	0.72579
(4-5)/6	0.37044	0.02425	0.66060	-0.35020	0.39981	0.20099	-0.17770	0.26706
(6-3)/6	-0.11356	-0.62486	0.02334	-0.10261	-0.11885	0.25672	0.58884	0.39852

B = Breadth, H = height, .L = length, and FB = frontal breadth. B-FB/H (in Table 1) was not included in the analysis because it was highly correlated with B-FB/L (r = 0.98).

References

S1. J. C. Dainty, R Shaw, *Image Science: principles, analysis and evaluation of photographic-type imaging processes* (Academic Press, New York, 1974).

S2. C. J. Connolly, *External Morphology of the Primate Brain* (Charles C. Thomas, Springfield, IL, 1950).

S3. A. Verioes, *Orphanet Encyclopedia* (online journal; http://www.orpha.net/data/patho/GB/uk-MVMSG.pdf), February (2004).

S4. A. Kumar *et al*., J. Biosci. **27**, 629.

S5. A. J. Barkovich *et al*., *Neurology* **57**, 2168 (2001).

S6. M. Henneberg, A. Thorne, in L. Barham (Ed) Some initial reactions to the publication of the discovery of *Homo floresiensis* and replies form Brown & Morwood. *Before Farming* (online journal) **4**, article 2 (2002).

S7. R. E. Passingham *New Scientist* **68**, 510 (1975).

S8. A. H. Schultz, *Primatologica* **I**, 887 (1956).

S9. R. E. Passingham *Brain Behav Evol* **7**, 337 (1973).

S10. R. E. Passingham, G. Ettlinger, in *International Review of Neurobiology*, C. Pfeiffer, J. Smythies, Eds. (Academic Press, New York, 1974), pp. 233-299.

S11. H. Stephan, R. Bauchot, OJ Andy, (1970) in *Adv Primatol vol 1, The Primate Brain*, C. R. Noback, W. Montagna, Eds. (Appleton-Century-Crofts, New York, 1970), pp. 289-297.

S12. V. Pennetti, L. Sgaramella-Zonta, P. Astolfi, in *African Pygmies*, L. Vavalli-Sforza, Ed. (Academic Press, New York, 1986), pp. 127-138.

S13. A. Walker, R. Leakey, *The Nariokotome Homo Erectus Skeleton* (Harvard University Press, Cambridge, 1993).

S14. P. Brown *et al*., *Nature* **431**, 1055 (2004).

S15. L. L. Cavalli-Sforza, in *African Pygmies*, L. L. Cavalli-Sforza, Ed. (Academic Press, New York, 1986), pp. 81-93.

S16. B. T. Shea, R. C. Bailey, *Am. J. Phys. Anthropol.* **100**, 311 (1996).

S17. D. Falk *et al*., *J. Hum. Evol*. **38**, 695 (2000).

S18. D. Falk, *Primate Diversity* (W. W. Norton, New York, 2000).

S19. R. L. Holloway, D. C. Broadfield, M. S. Yuan, *The Human Fossil Record, Volume Three, Brain Endocasts-The Paleoneurological Evidence* (Wiley-Liss, Hoboken, New Jersey, 2004).

S20. D. Falk, *Nature* **313**, 45 (1985).

S21. D. Falk, *Yrbk Phys Anthropol* **16**, 13 (1987).